RoboFly: An Insect-sized Robot with Simplified Fabrication that is Capable of Flight, Ground, and Water Surface Locomotion

Yogesh M. Chukewad¹, *Member, IEEE*, Johannes James², *Student Member, IEEE*, Avinash Singh³, and Sawyer Fuller², *Member, IEEE*

Abstract—Insect-sized (~ 100 mg) aerial robots have advantages over larger robots because of their small size, low weight, and low materials cost. Previous iterations have demonstrated controlled flight but were difficult to fabricate because they consisted of many separate parts assembled together and were also unable to perform locomotion modes besides flight. This paper presents a new design of a 74 mg flapping-wing robot that dramatically reduces the number of parts and simplifies fabrication. The robot also has a lower center of mass, which allows the robot to additionally land without the need for long legs, even in case of unstable flight. We also show that the new design allows for wing-driven ground and air-water interfacial locomotion, improving the versatility of the robot. During surface ambulation, forward thrust is generated by increasing the speed of the upstroke relative to the downstroke of the flapping wings. Adjusting relative wing stroke amplitudes also allows for steering. The ability to land and subsequently move along the ground first presented here allows the robot to negotiate extremely confined spaces and underneath obstacles. We present results demonstrating these capabilities, as well as hovering flight and controlled landing.

Index Terms—Insect-scale Flapping-Wing Robot, Aerial Systems: Mechanics and Control, Ground Locomotion, Air-Water Interfacial Locomotion, Micro-fabrication.

I. INTRODUCTION

¹Yogesh M. Chukewad is with Unchained Labs, 6870 Koll Center Pkwy, Pleasanton, CA, 94566, USA (e-mail: yogeshc@uw.edu)

³Avinash Singh is with Fresh Consulting, 14725 SE 36th st, ste 300, Bellevue, WA 98006, USA (e-mail: avinsh@uw.edu)

Corresponding author: Yogesh Chukewad

Manuscript received Month XX, 20XX; revised Month XX, 20XX.

losses such as Coulomb friction and electrical resistance take on greater importance as scale reduces [2]. Recently, however, a suitable manufacturing process and actuation technology were demonstrated that allowed for controlled flights in an 81 mg robot [3]. This robot was built using a diode-pumped solid-state laser and pin-aligned sheet adhesion to fabricate the necessary components [4], and was actuated by piezo-driven flapping wings that emulated the motion of insects [5]–[8]. The mechanism required to convert the actuator motion to wing motion for generating aerodynamic lift is discussed in [9], in which transverse bending of wings as observed in insect flapping is investigated for efficient flapping.

This paper addresses three deficiencies of the basic design introduced in [3], introducing a new design that makes robot flies both more versatile and easier to fabricate.

- 1) Complex fabrication: The insect robot design of [3] suffers from being very difficult to fabricate because it requires hand assembly of a relatively large number of discrete components. It also consists of several failure-prone steps. An alternative was proposed in [4] that reduced the number of parts by taking inspiration from children's pop-up books. A robotic fly design was demonstrated that consisted of a fabrication step that required actuating a mechanism with only a single degree of freedom. But this design approach is complex, requiring 22 layers with many interdependencies between layers.
- 2) Difficulty in landing: The work in [3] demonstrating controlled flight by an 81 mg robot relied on feedback control of its upright orientation using retro-reflective marker-based motion capture. When upright, its long axis extends vertically, raising its center of mass and making it challenging to achieve a successful landing without toppling over. Successful landings with that design required leg extensions that nearly doubled the vehicle's size [10]. An alternative is to use switchable electrostatic adhesion [11] for perching and takeoffs on vertical or overhanging surfaces, but this adds complexity including a high-voltage source, requires a small amount of additional power to remain attached. The electrostatic adhesion relies on a high-voltage difference (1200 V) between the electrodes, which is significantly different from the 200-300 V needed by the piezoelectric actuators used to actuate the wings in this work. This suggests that electrostatic landing requires incorporating an additional high-voltage source, also adding

² Johannes James and Sawyer Fuller are with the Department of Mechanical Engineering, University of Washington, Seattle, WA, 98105 USA. (e-mail: jmjames@uw.edu; minster@uw.edu)

mass to the vehicle.

3) Limited mobility autonomy: Mobility autonomy for terrestrial robots can be defined as the ability to traverse unknown and non-smooth terrain according to [12]. Here, we define mobility autonomy for insect scale robots as their ability to traverse locomotion with multiple modes which involve aerial, terrestrial, and aquatic locomotion. There have been significant developments in small scale robotics, including a 1 g miniature water strider robot [13], a robot that can jump from the surface of water [14], a 1.6 g underwater quadrupedal robot [15], and a 175 mg flying robot capable of making the transition from water to air [16]. Here, to avoid actuators contacting water, we focus on the locomotion on the surface of the water.

A 165 mg flapping-wings water-skating robot is demonstrated in [17]. However, this robot cannot perform aerial locomotion since it propels only in the horizontal plane. The work in [16] demonstrates an aerial-aquatic flight that relies on a sparker while performing the transition from water to air. Though this robot can move itself underwater, it requires deionized water to avoid short-circuit and accidentally breaking actuators. Most bodies of water are not this pure, and conduct electricity, causing sudden transient arcs and actuator breakage, requiring a perfect seal on the actuators. Multi-modal locomotive capabilities have been widely studied for biological species such as water striders that rely on surface tension to support their weight. An investigation of the dynamics of water walking creatures is presented in [18]-[20]. Hydrodynamics of water walking arthropods with characteristic length of the order 1 cm is presented in [18] and [19]. Propulsion mechanism in water striders, as presented in [19], includes momentum transfer through capillary waves and hemispherical vortices created by the driving legs. Various means of weight support at the water surface, as well as lateral propulsion for various water-walking creatures (not limited insects scale), are discussed in [20]. Propulsion mechanisms presented in the work include: 1) surface slapping (lizards), 2) rowing and walking (most of the water insects), and 3) meniscus climbing (Pyrrhalta nymphaeae larvae and Mesovelia). A quantitative biomechanical model of insects' interfacial flight is presented in [21], along with an investigation of water-lily beetles' interfacial flights. It was shown that the interfacial flight is energetically expensive as compared to aerial flights. While above-mentioned research focused on aquatic locomotion of biological creatures, the review by Kwak and Bae in [22] connects the biology with robotics by identifying robotic research in aquatic locomotion that can draw inspiration from its biological counterparts.

In light of the above limitations in fabrication, landing and mobility autonomy in previous designs, this paper describes a new design of an insect-sized flying robot, which we call RoboFly (Fig. 1), that is intended to overcome the deficiencies of previous designs described above. Current paper evolves from authors' earlier conference paper [23], which focused on the design and fabrication of the RoboFly, and its capability to perform open-loop landing and ground locomotion. The current submission represents a significant advance over the earlier paper. It, in addition to earlier results, demonstrates how the robot can be modified with a set of passive legs to

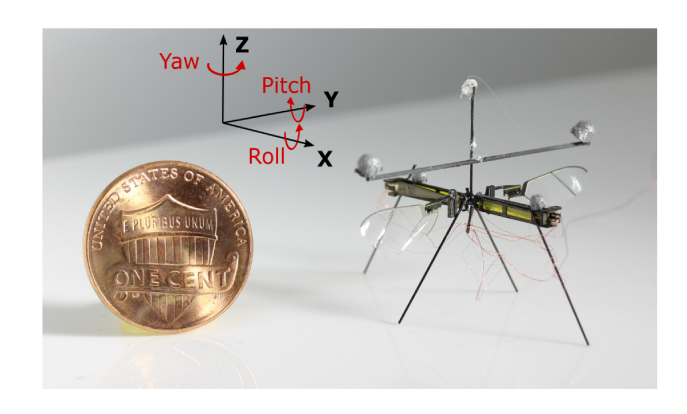


Fig. 1. The redesigned system: RoboFly. Each wing measures 13 mm in length and is driven by a separate piezoelectric cantilever actuator. By extending the actuators forward and aft (along X-axis), the center of mass is positioned near the base of the wing pair so that there is no net torque during flight. The entire robot weighs 74 mg (without retro-reflective markers). The robot's coordinate frame and angular motion axes are shown for reference. A US penny is shown for scale.

perform water-air interfacial locomotion. The earlier paper had demonstrated a stabilized takeoff; however, the current paper takes a step further to demonstrate a controlled hovering flight and closed-loop landing.

Here we report three main contributions to the design of the robot insects, which are embodied in the new design.

- This design introduces a fabrication process in which the basic wing actuation unit is composed of a multilayer composite sheet, simplifying fabrication relative to earlier designs.
- 2) This design has a lower center of gravity, which facilitates open-loop landing on the ground.
- 3) This robot also possesses better mobility autonomy with its ability to perform multi-modal locomotion which includes aerial, ground and water locomotion. The robot uses its wings to push itself along the ground and water once landed, without additional complexity and weight of a separate walking mechanism.

The rest of the paper is organized as follows. In section II, we introduce the new robot re-design and its simplified fabrication which significantly reduces the number of parts and improves the accuracy of the assembly. In section III, we discuss the ability of the robot to perform multi-modal locomotion, including aerial and ground locomotion. Results from experiments from ground and aerial locomotion are also presented. In section IV, we first provide the theory behind small floating objects. We also discuss the design of hydrophobic legs which can be attached to the robot to make it float on the water surface. We also present results from experiments from water locomotion and a transition from aerial to interfacial flight in which the robot lands on the water without breaking the surface tension film. In section V, we discuss the power consumption in the different locomotion modes.

II. ROBOFLY FABRICATION

In this section we discuss the basic design of RoboFly as introduced in [23]. This robot has served as a platform for

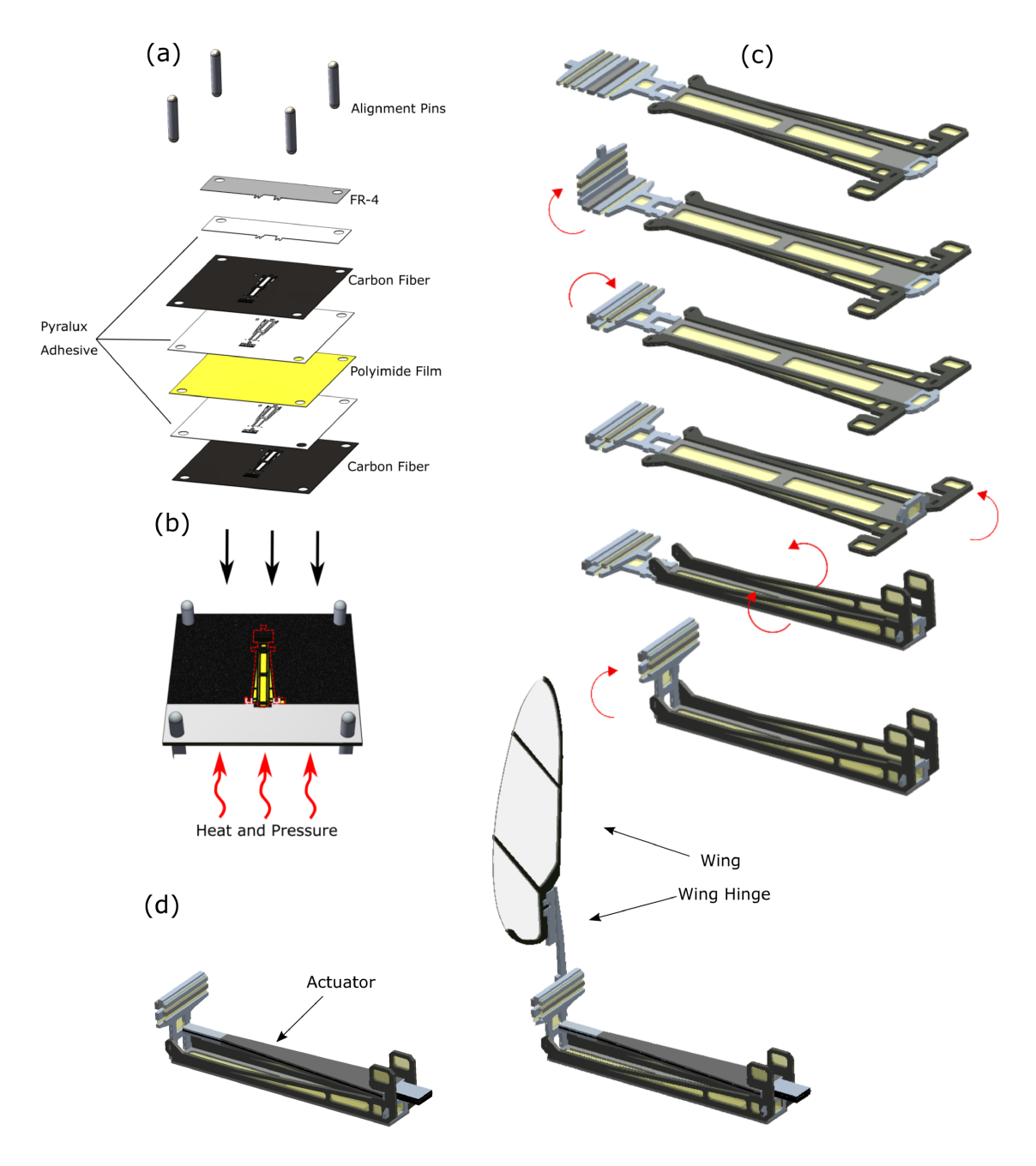


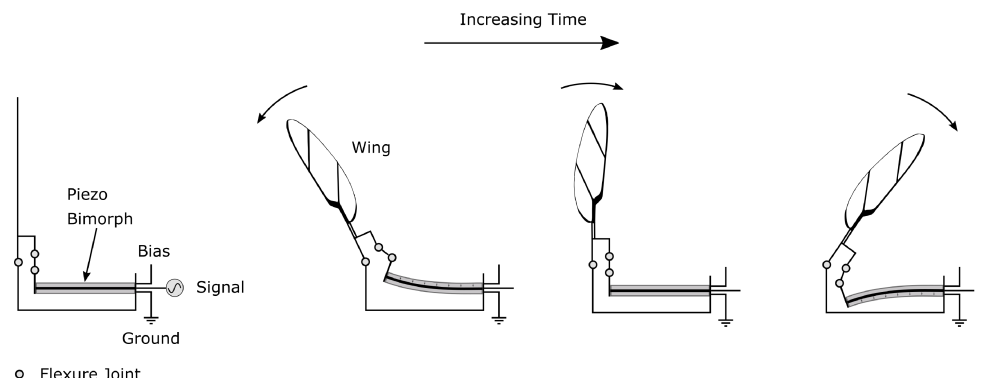
Fig. 2. (a) An exploded view of the layup before curing. (b) Layup during the curing process under predetermined pressure and temperature. Release cut to be done on the cured laminate is shown in red dotted lines. (c) The released laminate is shown at the top, followed by the process involving folding of transmission and the airframe. (d) (Left) An actuator is slid into its designated slot on the airframe, (right) wing with its hinge is attached on the transmission.

several studies, including wireless power circuit [24], a pinhole lens camera [25] on-board. Four half-flies are assembled in the work by [26]. In the current study, we focus on its design and consequent expanded locomotion capabilities.

RoboFly consists two identical subunits, each of which consists of a piezoelectric actuator, a carbon fiber airframe, and a wing. A set of four vertical legs are attached for landing and ground locomotion. The process of fabrication and assembly is explained in detail below.

Our design simplifies fabrication by combining the airframe, transmission, and actuator attachment hardware into a multilayer composite sheet. In the previous design that performed controlled flight [3], these consisted many separate parts. Combining these into a single multi-layer composite sheet reduces the number of discrete parts and facilitates fabrication during prototyping. Many design features and alignment steps can be built into the design of the laminate. For example, the laminate consists of castellated folds [27] that impose a precise rotation axis, and mechanical interlocks that can constrain folds to a specific angle.

The laminate is machined and assembled using the following steps:



- Flexure Joint★ Electric Field Direction
- Electric Field Birection

Fig. 3. Diagram of the mechanism showing piezoelectric cantilever actuation of the wings the design presented in this work. The piezo actuator drives large-amplitude wing motion through small strain changes. The piezo actuator is configured as a bimorph cantilever, consisting of a carbon fiber layer sandwiched between top and bottom piezo sheets. The top surface of the bimorph is charged to a constant high voltage, while the bottom surface is tied to ground per "simultaneous drive" configuration. An alternating signal is connected to the middle layer, providing an alternating electric field in the piezo material. This produces alternating small strains through the reverse piezoelectric effect, which is manifested as motion at the tip of the cantilever. A microfabricated transmission amplifies these tip motions into large (~ 90 deg) wing motions. This diagram shows the mechanism as seen from above; motion of the wings causes airflow downward, into the page.

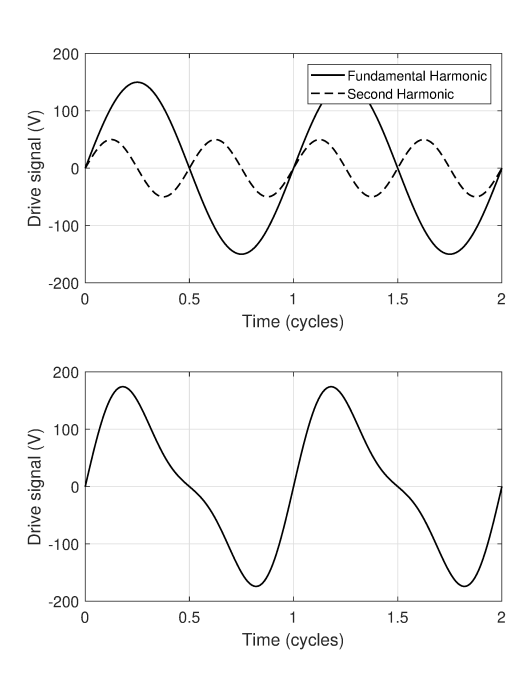


Fig. 4. The addition of a second harmonic signal causes a differential stroke speed. (top) The sinusoidal drive signal to the wings and the second harmonic at 0.3 times the fundamental amplitude. (bottom) The sum of the two signals. The value of μ is limited to the range [-0.3, +0.3] in order to avoid excessive distortion of the combined waveform from the fundamental harmonic.

- 1) Two carbon fiber composite sheets $(0^{\circ}-90^{\circ}-0^{\circ}$ sheets of 27 μ m thick cured prepeg) are laser machined using a diode-pumped solid-state frequency tripled Nd:Yag laser with 355 nm wavelength (PhotoMachining, Inc., Pelham, NH USA). These two sheets constitute the rigid structural material at the top and bottom of the composite layup.
- 2) A modified acrylic adhesive (FR1500 Pyralux, DuPont, Inc., Midland, MI) is laser machined with the same pattern as the respective carbon fiber layer features.

- 3) A layer of FR-4, a fire-resistant composite laminate, is introduced at the top of the laminate. This laminate acts a non-conducting layer between the actuator and the conducting carbon fiber layer. A layer of acrylic adhesive with the same pattern as the FR-4 layer is used between the top carbon fiber layer and FR-4.
- 4) A layer of 12.5 μ m polyimide film (Kapton) is laser cut and is placed between the two adhesive layers. The thickness of the Kapton film is chosen according to the flexure feature dimension of the transmission.
- 5) Polished stainless steel pins align these layers, ensuring that the features are placed correctly, as shown in Fig. 2 (a).
- 6) The layup is cured in a heat press at 200°C, 480 kPa (Fig. 2 (b)).
- 7) The layup is placed back in the laser system where it is re-aligned rotationally and in translation relative to the beam. Release cuts are machined as necessary. The release cut is shown with red dotted lines in Fig. 2 (b).
- 8) Each airframe-transmission part is folded by hand with tweezers under a microscope and bonded with cyanoacrylate adhesive (Fig. 2 (c)).
- 9) An actuator is then carefully placed and bonded to the slots provided on the airframe with extra material to insure a rigid connection at its base (Fig. 2 (d)).
- 10) A wing is bonded to a wing hinge, and the wing assembly is then attached to the transmission (Fig. 2 (d) (right)). As in [28], the wing hinge allows the angle of attack to change passively [29].
- 11) Two half-fly assemblies are bonded together at the middle on a specially-designed mating surface.
- 12) 30 μ m diameter carbon fiber rods are glued to the static surface of the transmission and at the front and back extremes of the body to form the legs.
- 13) A wire bundle consisting of four 51 AWG insulated copper wires is then carefully soldered onto the actuators' bases to complete the electronic connections.

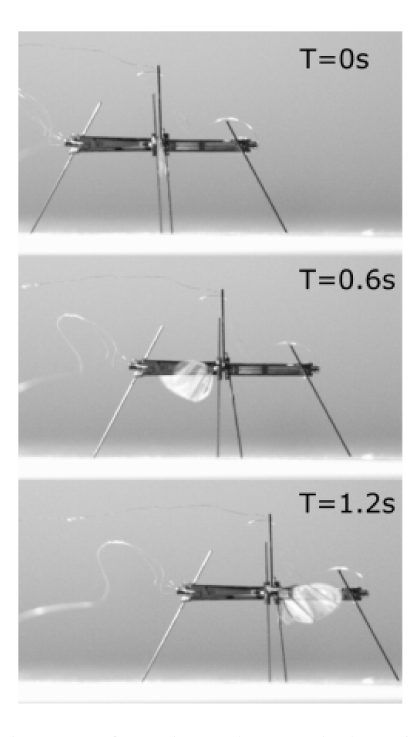


Fig. 5. The robot moves forward over the ground when wings are flapped faster in the backward direction than the forward direction. Flapping frequency 60 Hz. In the absence of a steering command, the robot moves in a straight line.

III. MULTI-MODAL LOCOMOTION

This section discusses experimental apparatus and results. First, we describe the operation of the robot and the hardware involved in the experiments, followed by experimental results of the robot performing different types of multi-modal locomotion.

A. Operation

The piezo actuators were driven by a desktop computer equipped with a digital-to-analog conversion board (NI 6259) running Simulink Real-Time (MathWorks, Natick, MA, USA) and amplified using three high voltage amplifiers (Trek 2205, Lockport, New York). One amplifier supplies the DC 'bias' signal to both actuators; the other two amplifiers each supply the separate sinusoidal drive signals to the two wings.

Ground locomotion is performed by flapping the wings at a lower frequency than is needed for flight but at similar stroke amplitude. Stroke amplitude is determined by the amplitude of the drive signal voltage (Figs. 3, 4).

The wing flapping frequency is varied depending on the mode of the locomotion that we want to carry out. However, it is kept constant for a particular mode which can be one of the following set of actions at any time instanceground locomotion, water locomotion, and flight. Maneuvers while performing these actions were carried out by varying the voltages at which the actuators are driven. All actions besides flight are performed at non-resonant frequency to avoid accidental lift-off. Each actuator is driven at a voltage signal, $V(t) = V_0 + A_0 \sin(\omega t) + A_1 \sin(2\omega t)$, where V_0 is the offset voltage, A_0 the amplitude, $A_1 = \mu A_0$ the amplitude for the

second harmonic term; a typical value μ ranges from -0.3 to 0.3. By adding a second harmonic at double the frequency, so that either the downstroke or upstroke is faster (Fig. 4), the robot is driven forward or backward as result of aerodynamic drag on the wings. For example, forward motion occurs when the signal to the wings drives them rapidly backwards. A similar mechanism was proposed to induce torques about a vertical or yaw axis in [3] and [30].

In case of aerial locomotion, the wings are flapped at resonant frequency to generate maximum lift. One way to determine the resonant frequency that maximizes the lift for flapping-wing micro aerial vehicles (FWMAV) is presented in [31], in which the authors performed the system identification of an FWMAV to fit a linearized second order model.

We hypothesized that forward motion on the ground is due to the robot momentarily exceeding coulomb friction during the fast period of the wing stroke.

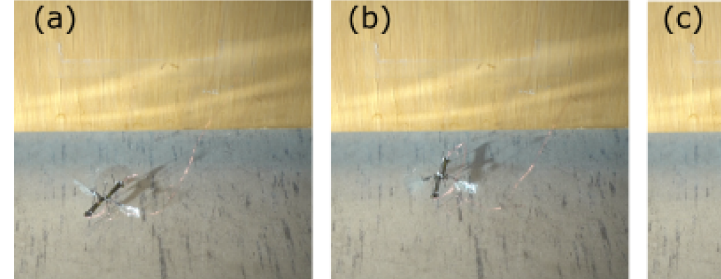
To determine whether this motion was primarily driven by inertial or by aerodynamic forces, we performed an experiment in which the wings were replaced by carbon rods with identical mass and moment of inertia. When supplied with driving signals that moved the robot when it was equipped with wings, it was observed that the robot with carbon rods did not move significantly from its initial position. This indicates that the forces causing the ground locomotion are mainly due to the aerodynamic drag acting on the wings. This also makes the robot distinct from other vibratory micro-robots [32]–[34] which rely on the vibration or inertial forces for ambulation. We also note that the Reynolds' number of the wing is approximately 3000 [28], that is, dominated by inertial forces. This indicates that drag is proportional to the square of the wing velocity according to $f_d = \frac{1}{2}C_D\rho Av^2$, where C_D is the aerodynamic drag coefficient, ρ is the air density, A is the frontal area of the wing, and v is the velocity of the wing. Therefore, a faster wingstroke with a higher v will produce higher drag than a slow stroke.

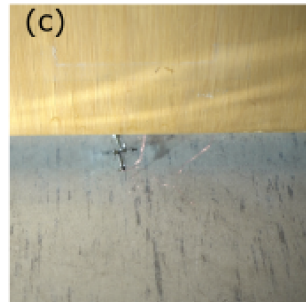
B. Ground Locomotion

Fig. 5 and the supplementary video [35] show the robot performing ground locomotion along a straight line. In these trials, the wings were flapped at a lower frequency of 60 Hz, but with an of amplitude of 210 V, which is similar to the amplitudes in other modes of locomotion. Fig. 6 and the video [35] show that ground ambulation allows the robot to navigate under a closed door.

To determine how the driving signal affects locomotion, the RoboFly was driven in the forward direction with a range of different voltages and frequencies. Displacements were measured with a ruler, and the speed was calculated by dividing by the time taken. The results show that robot velocity increases with increasing flapping frequency and amplitude (Fig. 7). We conjecture that the large velocity increases that occur at different amplitudes are the result of the robot overcoming coulomb friction at a critical phase of wing flapping. The small increase from 225 V to 250 V is likely attributable to the small resulting additional stroke amplitude.

Steering is performed by varying the signals given to each flapping wing independently. To steer the body to the left, the





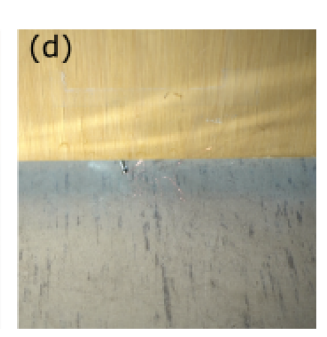


Fig. 6. Ground locomotion allows the robot to navigate under aerial obstacles. The robot is shown ambulating under a closed door, which would not be possible by flying.

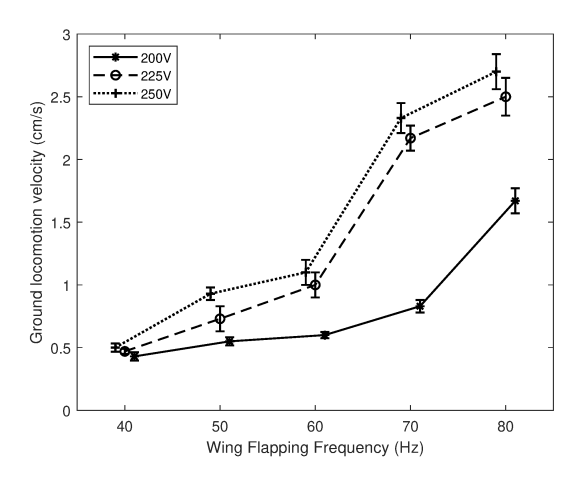


Fig. 7. Ground locomotion velocity increases with increasing signal amplitude and flapping frequency. For comparison, liftoff occurs at approximately 140 Hz.

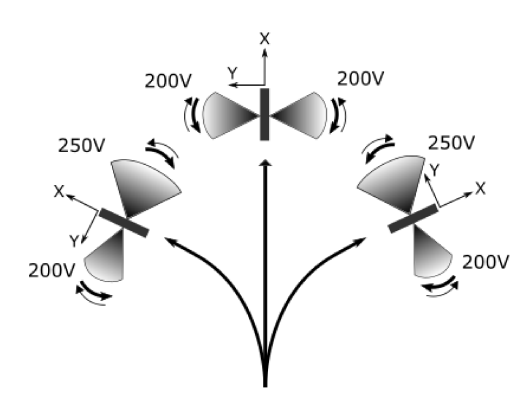


Fig. 8. A top view of ground locomotion and steering. Steering can be performed by driving the wings with unequal signals. Thickness of the arrows corresponds to the stroke speed. Here, the rearward stroke is faster than the forward stroke, causing larger drag during rearward stroke, thereby achieving forward motion. Modulating flapping amplitude in addition to differential stroke speed can be used to achieve the steering torque (moment about Z-axis) in addition to forces along forward-aft (X) axis. Local coordinate frames are shown at the front of the robots. Z-axis is perpendicular to the plane of the paper.

left wing is flapped at a reduced drive signal amplitude relative to the right wing (Fig. 8). The rate of rotation is determined by the relative drive signal amplitude difference in the two wings. A sharp turn can be achieved by keeping one wing stationary while the other wing flaps. The extreme continuation of this would be rotation about a vertical axis passing through the center of the body, for which the wings are flapped 180° out of phase. A continuous range of turn angles can be achieved by modulating the difference between left and right wing drive signals.

Fig. 9 and the supplementary video [35] show that the robot is able to steer in addition to moving forward. Here, the wings were flapped at 70 Hz as above, but the left wing was flapped with larger drive signal amplitude (250 V) whereas the right wing was flapped at a lower value (200 V). Similarly, the robot was observed to steer in the other direction when these amplitudes were reversed. Moving backwards was also achieved using the appropriate driving signals.

C. Takeoff and Flight

Hovering at a specified location in space was performed using feedback from a motion capture (MoCap) system (four Prime 13 cameras, OptiTrak, Inc., Salem, OR) which tracks retroreflective markers attached on the robot. This MoCap system sends position and orientation information over Ethernet at 240 Hz to the host desktop computer which runs Simulink Real-Time.

RoboFly is an under-actuated system. However, it can move to any point in space by changing its attitude and tilting the thrust vector in the desired direction of motion. For altitude control the robot uses a proportional-integral-derivative (PID) controller to achieve desired height. The controller used by the robot for position control is shown in the block diagram in Fig. 10. The MoCap system, through the host computer, continuously sends the position and orientation data over the ethernet to the Simulink Target computer which runs the controller. When the controller is fed with the reference point $[x_d(t), y_d(t), z_d(t)]^T$, it varies the signal amplitude to react to the error in altitude, as mentioned above. At the same time, the controller varies the wing signal according to two control loops— inner attitude loop and outer lateral position loop, as shown in the block diagram.

As for the altitude controller which runs in parallel with the attitude controller, the height of the robot is controlled using a PID controller. The thrust generated by the wings of the robot is approximately linear with the wing amplitude. Vertical acceleration can be written by the control law as follows:

$$a_z = k_{ph}e_z + k_{dh}\dot{e}_z + k_{ih}\int_0^t e_z dt \tag{1}$$

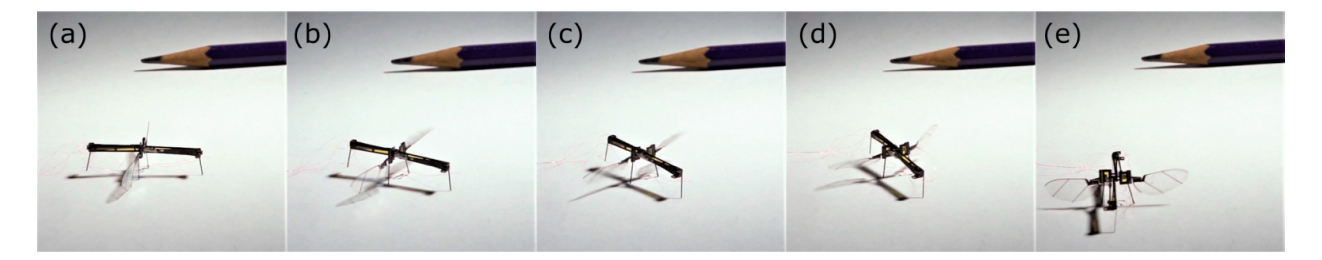


Fig. 9. Robot turns right by 90°. A pencil tip is shown in the background for scale.

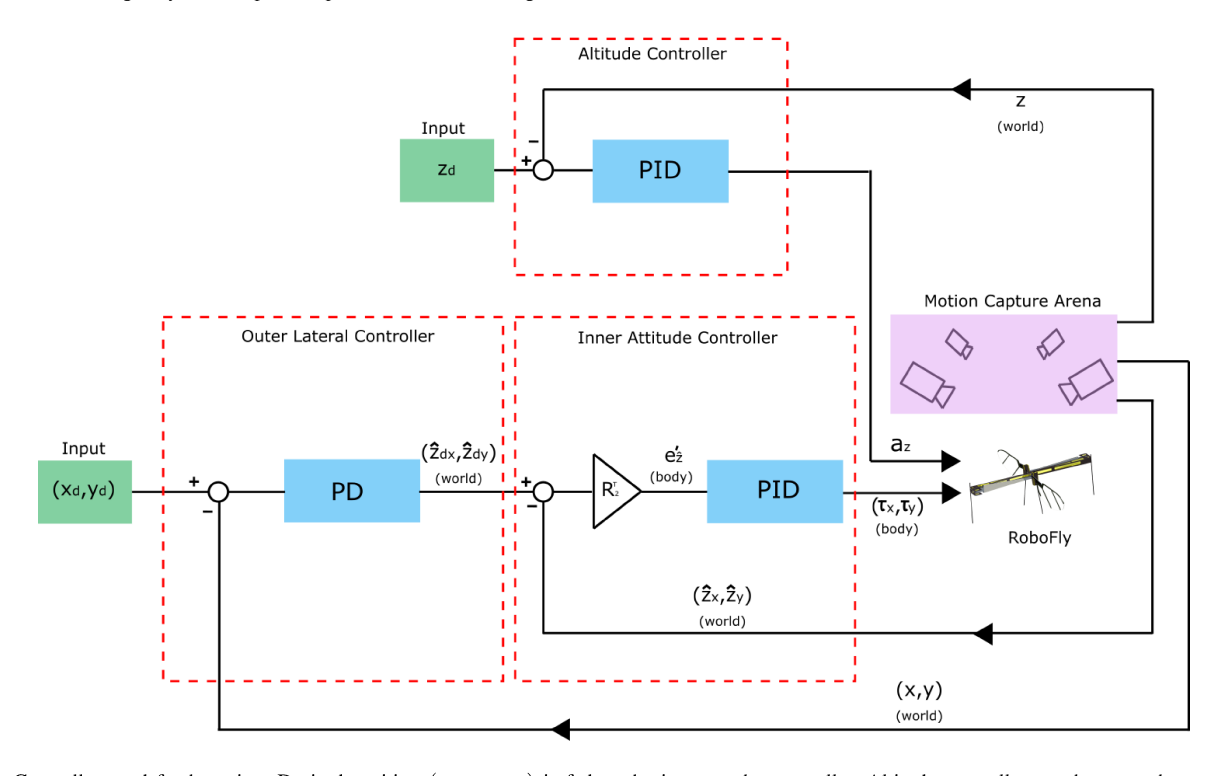


Fig. 10. Controller used for hovering. Desired position (x_d, y_d, z_d) is fed as the input to the controller. Altitude controller, as shown at the top, achieves desired altitude z_d by generating vertical acceleration a_z . The lateral position controller works on the desired lateral coordinates to compute desired thrust vector orientation, which is fed into the inner attitude controller which determines roll and pitch torques (τ_x, τ_y) . Motion capture system which tracks the position and orientation of the robot is used for the feedback.

where $e_z=z_d-z$ is the error between desired height z_d and current height z; k_{ph} , k_{dh} and k_{ih} are proportional, derivative and integral gains, respectively. z values received from the MoCap system are first filtered using a low-pass Butterworth filter before taking derivatives. The Butterworth filter, which is a low-pass filter designed for a flat frequency response in the desired frequency range, has been widely used for filtering sensor data [26], [36], [37]. We used a third-order Butterworth filter with a cut-off frequency equal to the update rate of the MoCap system (240 Hz).

As for the cascaded lateral and attitude controllers, the outer loop receives the current and desired lateral positions in the world coordinate system. The error goes through a proportional-derivative (PD) controller, which generates a desired change in attitude vector trajectory $\hat{\mathbf{z}}_{\mathbf{d}}(\mathbf{t})$ which is fed into the inner attitude control loop. $\hat{\mathbf{z}}_{\mathbf{d}}(\mathbf{t})$ is termed as the desired inclination trajectory in the rest of the paper, since it is the trajectory of the desired inclination of the thrust vector, $\hat{\mathbf{z}}$ in world coordinates. The outer loop assumes that the inner

loop responds to attitude changes almost instantaneously.

In the outer loop, the lateral position of the robot is controlled by determining the desired inclination trajectory $\hat{\mathbf{z}}_{\mathbf{d}} = [\hat{z}_{dx} \ \hat{z}_{dy}]^T$. This is performed by a PD controller in the world coordinate system:

$$\hat{\mathbf{z}}_{\mathbf{d}} = \begin{bmatrix} \hat{z}_{dx} \\ \hat{z}_{dy} \end{bmatrix} = k_{pl} \begin{bmatrix} x_d - x \\ y_d - y \end{bmatrix} + k_{dl} \begin{bmatrix} \dot{x}_d - \dot{x} \\ \dot{y}_d - \dot{y} \end{bmatrix}, \qquad (2)$$

where (x, y) and (x_d, y_d) are the current and desired lateral positions in global coordinate system, respectively; k_{pl} and k_{dl} are the proportional and derivative gains, respectively.

In the inner loop, attitude is controlled by rotating the robot's thrust vector towards the desired lateral position. In other words, objective of the inner loop is to align the thrust vector $\hat{\mathbf{z}} = [\hat{z}_x \ \hat{z}_y]^T$ along the desired inclination trajectory $\hat{\mathbf{z}}_{\mathbf{d}}$. So far we have everything in the world coordinate system; however, desired roll and pitch torques need to be determined in body-attached frame.

The robot's attitude is parameterized by a rotation matrix ${\bf R}$ that relates body and world coordinates according to ${\bf v}={\bf R}{\bf v}',$ where we define ${\bf v}$ to be any vector expressed in world coordinates, and ${\bf v}'$ is the same vector expressed in body-attached coordinates. The matrix ${\bf R}$ and body angular velocity ${\bf \omega}'$ were computed from the quaternion representation provided by the motion capture system. The error $e_{\hat{\bf z}}'$ between desired trajectory and the current thrust vector position, in body-attached frame is determined as follows:

$$\mathbf{e}_{\hat{\mathbf{z}}}' = \begin{bmatrix} e_{\hat{z}x}' \\ e_{\hat{z}y}' \end{bmatrix} = \mathbf{R}_{2}^{T} \left(\begin{bmatrix} \hat{z}_{dx} \\ \hat{z}_{dy} \end{bmatrix} - \begin{bmatrix} \hat{z}_{x} \\ \hat{z}_{y} \end{bmatrix} \right), \tag{3}$$

where \mathbf{R}_2 is the upper-left 2×2 block of the rotation matrix \mathbf{R} .

The inner faster loop for determining the roll and pitch torques in body-attached frame works as follows:

$$\begin{bmatrix} \tau_x \\ \tau_y \end{bmatrix} = k_{pa} \begin{bmatrix} -e'_{\hat{z}y} \\ e'_{\hat{z}x} \end{bmatrix} - k_{da} \begin{bmatrix} \omega'_x \\ \omega'_y \end{bmatrix} + k_{ia} \int_0^t \begin{bmatrix} -e'_{\hat{z}y} \\ e'_{\hat{z}x} \end{bmatrix} dt, \quad (4)$$

where k_{pa} , k_{da} and k_{ia} are the proportional, derivative and integral gains, respectively. Note that in this controller, torque about the x-axis depends on inclination along the y-axis and vice versa. The attitude error is the difference between desired and actual inclination. If the robot is facing in the world x-direction, the y-direction will be towards the left of the robot. In a situation where the lateral reference point in on the right of the robot, the attitude error vector will have a component in -y direction. It will require the robot to perform positive roll about body x axis. This justifies the negative sign with $e'_{\hat{z}y}$ in the above expression.

The controller described above produces a thrust a_z and torques τ_x and τ_y that are normalized by body mass and moment of inertia, respectively. To map these accelerations into voltage values supplied to the piezoelectric actuators. We assume that the thrust force is linearly proportional to amplitude. To estimate the moment arm for computing torques, we approximately determined the distance between the center of mass and the aerodynamic center of thrust for individual wing, using CAD model of the robot. The yaw motion of the robot is left uncontrolled in these experiments, as it does not affect the lateral and vertical control of the robot.

We demonstrated controlled takeoff in Fig. 12. Frames from a hovering flight are shown in Fig. 13 where the robot was flown for around 2 seconds. The 3-dimensional trajectory plot of this flight is shown in Fig. 14 (a). The robot was commanded to fly at a height of 4 cm from the starting point. It can be seen in Fig. 14 (b) that the robot successfully maintained the height at approximately 4.5 cm from the takeoff point. The RMS position errors during the last one second of the flight were 1.8, 1.75, and 0.5 cm for its x, y, and z positions, respectively.

D. Landing

One of the objectives of the re-design reported in this work was to give the robot the capability of landing upright even in the event of loss of control, without the need of long extended-out legs as in [39]. An upright landing allows for an easy

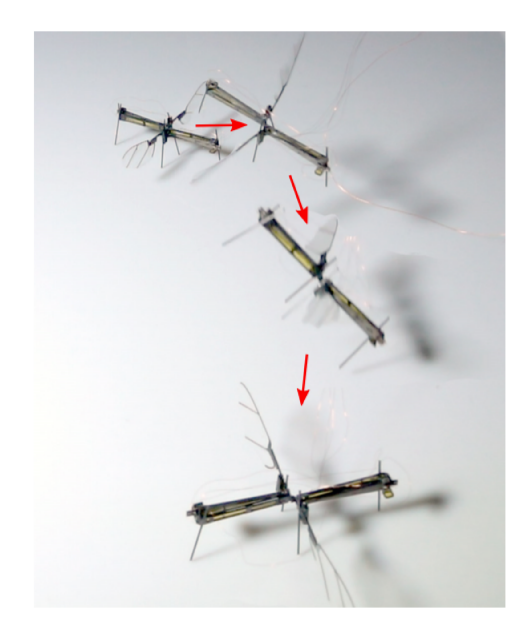


Fig. 11. A demonstration of open-loop takeoff and landing.

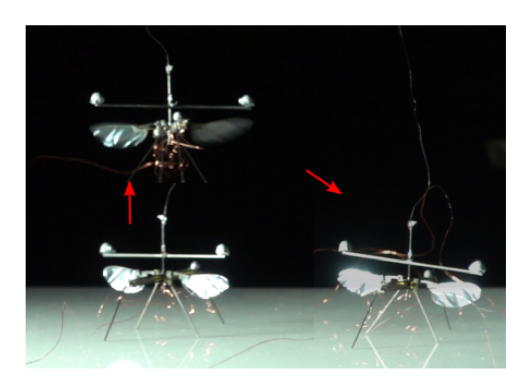


Fig. 12. A demonstration of closed-loop takeoff and landing.

transition to the next desired task, such as walking, sensing, or subsequent flights. This is facilitated by our robot's low center of mass, which makes it harder for the robot to topple.

We demonstrated an uncontrolled takeoff as shown in Fig. 11. In this video, the robot is seen to be flying with unstable attitudes and landing shortly after. Under feedback control, the robot remains approximately level as shown in Fig. 12. Under these conditions, the robot was able to perform a landing by gradually lowering the commanded altitude as shown in Fig. 14 (c) which was plotted for another experiment where the robot was flown for a longer duration.

Additionally, we showed that the robot was able to land even when feedback control was not present, indicating that the lowered center of gravity of our design improves landing robustness (Fig. 11).

IV. LOCOMOTION ON THE SURFACE OF WATER

In this section, we show that by adding legs of the appropriate size and shape, the robot can gain an additional locomotion capability: air-water ambulation along the surface of the water.



Fig. 13. Flight in which the robot takes off and hovers about a reference point in space with the help of feedback from a motion capture arena. The robot is subject to a small yaw bias torque that caused it to rotate leftward in this video [38].

TABLE I

COMPARISON OF NUMBER OF LAYERS AND DISCRETE PARTS REQUIRED IN
DIFFERENT CONSTRUCTION METHODS FOR CREATING INSECT-SIZED
FLYING ROBOTS

	Ma [3]	Sreetharan [27]	This work
Number of Layers:	5	22	7
Number of Distinct Parts:	14	1	8

A. Biological waterstriders

Our design is inspired by insects, such as stoneflies and mayflies, that use their flapping wings to push themselves along the air-water interface [21]. Like these animals, our robot moves along the surface by propelling itself with its flapping wings. Compared to an airborne RoboFly [23] which has six spatial degrees of freedom, an interfacially flying RoboFly has only three degrees of freedom because it is constrained to move along a surface. However, the surface tension forces acting on the legs of the RoboFly still makes it difficult to model the locomotion. Mukundarajan et al. [21] presented a dynamic model for an interfacial flight for actual biological insects. According to this model, forces acting on an actual biological insect performing interfacial flight are as follows: 1) horizontal air drag acting on the wings, 2) horizontal capillarygravity wave drag, 3) water drag acting on the legs at the contact with the water surface in the opposite direction to that of the motion, 4) body weight in vertical direction, 5) vertical resultant force due to surface tension, and 6) vertical water drag. The static case of the RoboFly locomotion is presented in this section.

In case of an object not moving or oscillating vertically, it can float on the water surface if its weight is balanced by the sum of two types of forces exerted on it. The first of these forces is buoyancy force. According to Archimedes'

principle, the buoyancy force exerted on an object is equal to the weight of the water displaced. Therefore, objects with density lower than that of water tend to float, and those with density larger than that of water sink. Water-walking arthropods have density larger than water, and therefore they would sink unless supported by the second type of force which is due to the surface tension of water. This force due to the surface tension is defined as the curvature force. The fluid surface deforms because of the weight of the insects, and this deformation in the fluid surface film leads to the curvature force. These forces on floating objects are explained in detail in the following subsection on legs design.

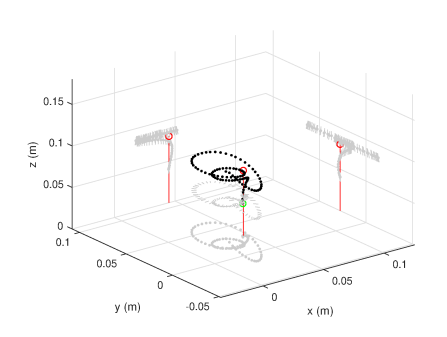
B. Supporting legs design using static analysis

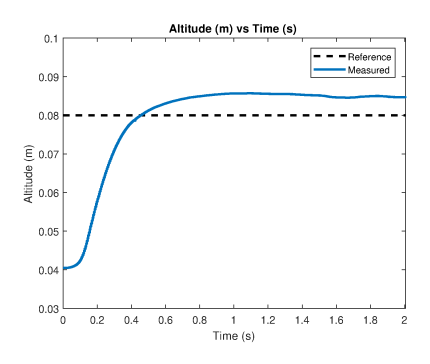
Legs play an important role in keeping the RoboFly on the water surface without breaking the surface tension film. Rigid and compliant legs were considered in [13]. However, that study was conducted on a robot which used actuating legs for propulsion. Here, we explore the use of wings for propulsion. Therefore, to keep the design simple, a rigid and passive set of three horizontal legs are attached to the RoboFly. These legs lie in the same plane at its bottom so that every part of the legs is in contact with the ground when placed on a flat surface. Cylindrical rods are chosen over square cross-section ones for the legs to avoid complication arising due to a potential case where the robot rests or lands on an edge of a leg. A simple configuration of three parallel legs is considered for this study.

Once we know the configuration and shape of the legs, next design parameters to be considered are 1) material, 2) diameter, 3) length, and 4) distance between the rods.

The diameter of the legs plays an important role in determining the ratio of buoyancy force and curvature force. The capillary length l_c , as shown in Fig. 15 (a) is independent of the leg diameter and contact angle. To keep the surface unbroken it is important to have the curvature force significantly larger than the buoyancy force. A carbon fiber rod of diameter 0.5 mm was chosen for the legs. This diameter corresponds to a Bond number, $Bo \approx 0.0092$, as calculated later in this section. Legs made out of stainless steel were used in [13]. Here, carbon fiber rod was chosen for its strength-to-weight ratio: it weighs about 3.6 mg/cm, whereas a stainless steel rod of the same diameter weighs about 15 mg/cm. Since the goal of this robot is also to perform multi-modal locomotion which includes flying, it is important to minimize mass.

While determining the length of legs, it is important to understand the forces acting on the legs while resting on the water surface. Surface tension causing curvature force is assumed to be the primary source of support to balance the weight. Buoyancy forces are not significant for the floating bodies of sub-gram weight, which is also demonstrated in [15]. Buoyancy force depends on the volume of water displaced because of the floating body [40], [41], and it corresponds to volume V_b as can be seen in Fig. 15 (a). Curvature force, on the other hand, corresponds to volume V_m displaced outside the contact line [40], [41]. This volume V_m depends on the capillary length, l_c , which is determined as $l_c = (\sigma/\rho g)^{0.5} \approx 2.6$ mm for objects floating on water surfaces, where σ and





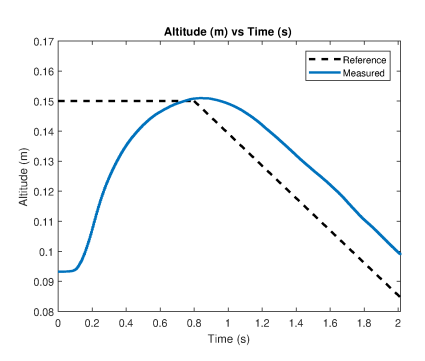


Fig. 14. (a) Trajectory plot of RoboFly taking off and hovering about an aerial reference point. This plot corresponds to the video from which the frames in Fig. 13 are taken. (b) Measured and reference altitudes vs time from the hovering experiment discussed above. (c) Measured and reference altitudes vs time from the hovering experiment where the altitude is dropped linearly after some time to demonstrate the control over the altitude, which is essential for a controlled landing.

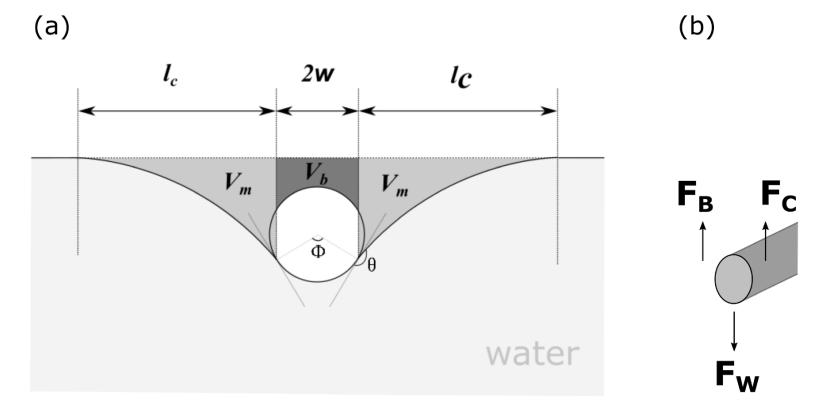


Fig. 15. (a) Schematic showing a static state of the cross sectional view of a horizontal leg of water-walking arthropod. w is the radius of the leg, l_c is the capillary length, θ is the contact angle, ϕ is the submerged angle, V_b is the water volume displaced inside the contact line and above the body, and V_m is the water volume displaced outside the contact line. (b) Vertical loads on the supporting legs. Here, F_C is the curvature force due to surface tension, F_B the buoyancy force, and F_W the weight distribution at the point of contact.

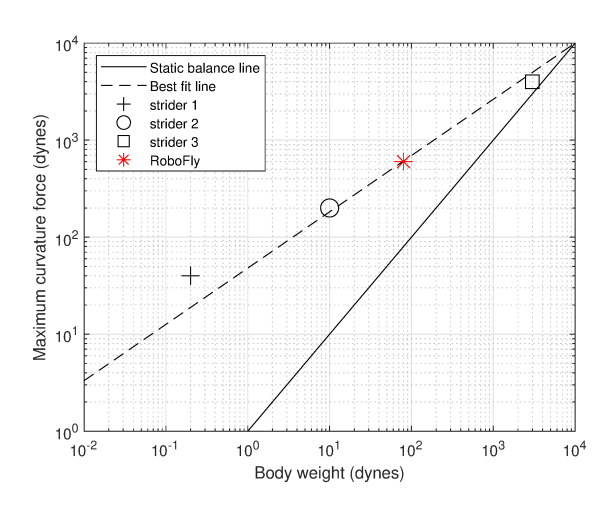


Fig. 16. The relation between maximum curvature force and body weight for 342 species of water striders as reported in [18]. The location of RoboFly is shown by a red star. Approximate locations of three water striders reported in [18] are also shown for comparison. The static balance line corresponds to the maximum curvature force required to statically balance the water striders at the water surface (maximum curvature force = body weight).

 ρ are coefficient of surface tension and density of water, respectively. According to [19], [40], [41], and Fig. 15 (a),

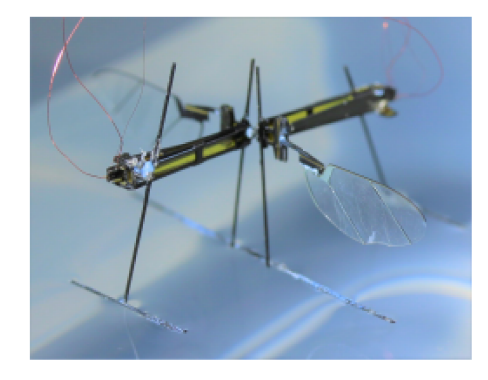


Fig. 17. The RoboFly design weighing ~ 95 mg and capable of performing multi-modal locomotion including aerial, ground, and air-water interfacial flights. Each wing is driven by a separate piezoelectric bimorph actuator. The surface tension force at the horizontal legs at the bottom supports the weight of the robot.

 $F_B/F_c \sim V_b/V_m \sim w/l_c = 0.25/2.6 = (Bo)^{0.5} << 1$. Therefore, we can assume F_c to be a significant contributor in supporting the robot at the surface. The above expression also gives us Bo, Bond number, equal to 0.0092.

For simplicity, we consider the weight F_W , as shown in Fig. 15 (b), to act uniformly along the entire length of all the three legs. In other words, we assume uniform weight

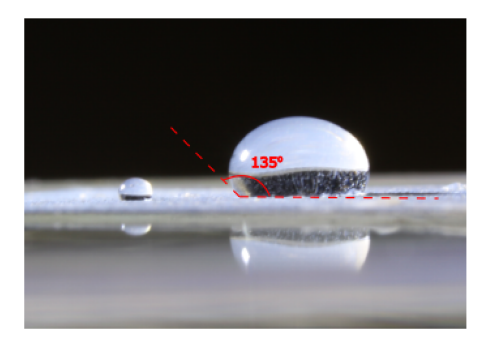


Fig. 18. Contact angle measured and shown on a steel shim coated with hydrophobic spray Rust-Oleum NeverWet

distribution on these legs. Let's, for a moment, assume the submerged angle ϕ , as shown in Fig. 15 (a), is equal to 90° . In that case, the curvature force in vertical direction F_c can be calculated as $F_c = 2\sigma L \cos(\theta)$, where L is the total length of the legs, and θ is the contact angle. From this expression, the maximum curvature force can be written as $2\sigma L$, which can be set equal to the weight to determine the minimum length of the legs, that turns out to be L_{min} =0.5 cm. However, this length of the legs is sufficient only when the entire supporting force due to surface tension acts in the vertical direction, which is not always the case. Also, the dimple due to a neighbouring leg can interfere with that of the one under study, which can reduce the supporting curvature forces as explained in [13]. Additionally, ripples that are generated due to the ground effect of flapping wings have unknown effect on the legs, and it can also reduce the supporting force at the interface. Because of these unknown effects, we turn to empirical study conducted by Hu et al. in [18]. A study of 342 species of water striders was conducted, and the relation between the maximum curvature force and body weight was found out [18]. The plot of the relation is shown in Fig. 16. The best fit line of the plot of this data was given by $max(F_c) = 48F_W^{0.58}$, where the forces are measured in dynes. Considering a 80 mg robot, $max(F_c) \approx 600$ dynes, which corresponds to $L \approx 4.2$ cm. This length of legs will add an extra mass of ~ 15 mg to the robot, which is compensated by further changing the total length of legs to 5 cm. So, the set of horizontal legs now consists of three pieces with the center one 2.5 cm long and other two 1.25 cm each. RoboFly is also compared with other water striders in Fig. 16.

Special attention is given to the minimum distance between two adjacent legs. If they are too close, the dimple caused by a leg on the water surface will interfere with that by its neighbouring legs. This will reduce the lift force generated by the surface tension at the contact with legs, this is shown in the study by [13] about the deformed water profile reducing the lift force. For a static case, it can be seen in their work that the dimple dies down at about 6 mm from a floating object, which requires us to have at least 12 mm of gap between legs. Keeping that in mind, we choose to have them 15 mm apart to be in safe situation in dynamic case in which the robot will be performing water locomotion.

C. Experimental results

The signal generated in this case is similar to the one used for ground locomotion. When the wings are flapped, ripples can be seen generating and propagating away from the robot on the water surface. Though the effect of ripples is unknown on the motion of the robot, it is observed that the robot doesn't move in any direction when the two wings are driven by the same driving signal without any second harmonic component. It can be concluded that the ripples have equal effect in all directions, and thus can be ignored in the dynamic force balance in the horizontal plane.

RoboFly with its horizontal legs is shown in Fig. 17. The design parameters for the legs are summarized in Table II. As mentioned in above section, RoboFly has the capability to move in either direction. Frames captured from a video of RoboFly moving from left to right are shown in Fig. 19. The robot in this video was driven with a second harmonic signal of amplitude 220 V, and the wings were flapped at 35 Hz, far below its resonant frequency. The recorded speed of this interfacial flight was ≈ 0.5 cm/s. We made sure that the copper wires have enough slack while floating on the water surface. To minimize the effect of these wire tethers, we used a set of four 51-gauge wires. To experimentally make sure that the wires' weight and deformation state didn't cause any forces due to pushing or pulling, we commanded the robot to move in forward and backward directions. No significant difference between the locomotion speeds was observed.

In addition to the straight-line motion, the robot can also steer by flapping one wing at a larger amplitude than the other. The robot can be seen taking a sharp turn towards left in Fig. 20 by flapping the right wing at a larger amplitude (220 V) than the left one (180 V). The angular speed is recorded as $\approx 20^{\circ}$ per second. Fig. 21 shows a set of images in which an airborne robot is seen to be landing on the water surface. In this uncontrolled flight, the robot simply jumps off the cardboard box in the background. It can be seen that the robot didn't land in its stable orientation; however, it still manages to recover without breaking the surface tension of the water. This may be attributed to the length of the legs being inspired by the actual biological species which may not have all the legs touching the water surface all the time. The length of the copper wires was chosen in such a way that they were never in tension while the robot landed and moved on the water surface. To further ensure that the copper wires have no role in the water-surface landing, we carried out more experiments in which we manually dropped a robot without copper wires from various heights. Three of those landings are shown in [42]. We observed that the robot was able to show the successful landing behavior consistently when dropped from lower than 3 cm height. The percentage of successful landings went down as the dropping height increased. Stabilized attitude and controlled descent are therefore essential to consistently achieve the water surface landing. Fig. 14 (c) shows that the robot can closely follow the input height trajectory.

TABLE II
SUMMARY OF DESIGN PARAMETERS OF LEG

Design Parameter	Value/Characteristic/Name	
Number of legs	3	
Cross-section	Cylindrical	
Material	Carbon fiber	
Diameter	0.5 mm	
Total Length	50 mm	
Distance between adjacent legs	15 mm	
Hydrophobic Coating	Rust-Oleum NeverWet	
Contact angle	135° (Fig. 18)	

D. Challenges

When the robot tries to take off, it relies on the wing lift to generate enough thrust to break its contact with the water surface. Immediately preceding the contact breakage, the surface tension which pulls the robot back assumes its maximum value, $2\sigma L$. If we assume, in a failed attempt of take-off, the robot comes to a static position right before the contact breaks, the meniscus assumes the maximum height. For the static analysis at this position, we can set the buoyancy force F_B equal to zero as robot legs are at their maximum height on the water surface. This will reduce the equation of motion to as in (5).

$$F_L = F_W + F_{C,max} \tag{5}$$

Now, substituting $F_{C,max} = 2\sigma L$ and values of all the unknowns, we can see that the value of F_L corresponds to 800 mg of force, which is 10 times the weight of the robot. It is impossible for this insect scale robot to lift off with an additional load of 9 times its own weight. That means it has to rely on some external factor to break the contact with the water surface. This phenomenon can be attributed to the behavior that has been observed with its biological counterpart *nymphaeae*. These insects, as shown in [21], oscillates in the vertical direction as they generate lift only in the downstroke; therefore, the meniscus is observed to be assuming its maximum height during downstroke and maximum depth during upstroke. As nymphaeae are seen to be taking off after some time which varies from a fraction of seconds to a few seconds, once the oscillations assume large amplitudes and the inertia is large enough to break the surface.

In *nymphaeae* study, the required lift-to-weight ratio is observed to be q=3.4, whereas it is observed to be $q\approx 10$ in the case of its robotic counterpart. The transition from iterfacial flight to airborne flight with the help of induced oscillations is considered to be out of scope for this paper.

V. POWER CONSUMPTION

The cost of transport (CoT) is a useful metric to compare different modes of locomotion. CoT is defined as the energy expense per unit distance traveled, or equivalently the power required per unit velocity, as shown in Eq. 6. To calculate CoT for the robot, voltage and current supplied to the bimorph actuators was measured at a sampling frequency of 10 kHz,

from the voltage and current monitor outputs of the amplifiers (Trek 2205, Lockport, New York). The instantaneous power was time averaged over an integer number of wing strokes in order to compute the average power consumption of the robot.

In order to estimate power requirements for an untethered robot, we envision a linear half-bridge driver circuit such as demonstrated in [24], [43]. In comparison to the desktop amplifiers, the onboard linear actuator driver would add inefficiency which would increase power requirements above what we measure for the tethered robot powered by the desktop amplifiers. Therefore, to estimate the power requirements an untethered robot, reverse power from the center node of the parallel-connected bimorph actuator is zeroed when computing the integral of V, I_r in Eq. 6. This assumption reflects the reality for linear half-bridge piezo driver methods that during the part of the wing stroke in which the sinusoidal drive signal voltage is decreasing, positive charge leaving the center node of the actuator must be dumped to ground through the transistor elements of the driver, and that energy cannot be recovered to the high voltage bias rail or back to the boost converter power source. Alternate driver topologies which are capable of bidirectional power flow [44] or which implement the energy recovery discussed in [45], can be somewhat more efficient than this proposed linear driver, so the power consumption and CoT computed here provides an upper bound of power requirements. The integral of the measured voltage V and current I from the amplifiers represents the lower bound of predicted power autonomous robot requirements because that would assume perfect driver efficiency.

Eq. 6 shows the computation of the cost of transport (CoT), that is, the energy used per unit distance traveled. The measured power was integrated over time and divided by the estimated distance traveled by the robot as measured by the motion capture system.

$$CoT = \frac{\int VI_r \, dt}{S} \tag{6}$$

Where S is the 3D distance traveled, V is the driving voltage, and I_r is the measured current.

To measure CoT for ground ambulation, we set the driving amplitude to 250 V. The results show that the cost of transport decreases with increasing flapping frequency (Fig. 22). This is conjectured to be the result of two competing factors: 1) Electrical input power increases proportionally with driving frequency f because the actuators are principally a capacitive load with current $I \propto C \frac{\mathrm{d}V}{\mathrm{d}t}$; 2) The aerodynamic lift increases with f^2 for the same reason that drag does (Section III). Therefore, for small frequency increases the robot is expected to reduce contact friction during ambulatory and water-striding motion faster than the power requirements increase. Together these factors suggest an inverse proportionality between CoT and flapping frequency which is observed in Fig. 22.

Measurements also indicated the trend of decreasing COT with increasing frequency while the robot was in flight. The COT was measured in flights traversing 0.2 m as measured by motion capture while flapping at 140 Hz. The COT for flying locomotion was ~ 0.02 mJ/mm, which is $\approx 25 \times$ less than the most efficient ambulation. CoT is not an applicable metric



Fig. 19. RoboFly performing water surface locomotion with open loop control by flapping wings at 35 Hz, frames are captured at 0, 4, 8, and 12 s



Fig. 20. RoboFly performing water surface locomotion and turning left with open loop control by flapping wings at 30 Hz, frames are captured at 0, 1, 2, and 3 s

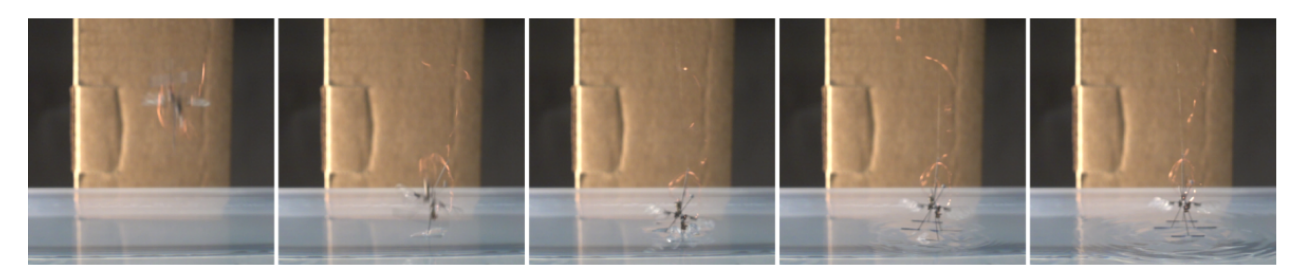


Fig. 21. Airborne RoboFly landing on the water surface. Frames are captured at 0 ms (robot is still airborne), 30 ms (landing only on front leg), 45 ms (middle leg also gets in contact with the water surface), 95 ms (all three legs are in contact now) and 145 ms (oscillations are damped and the robot is stable).

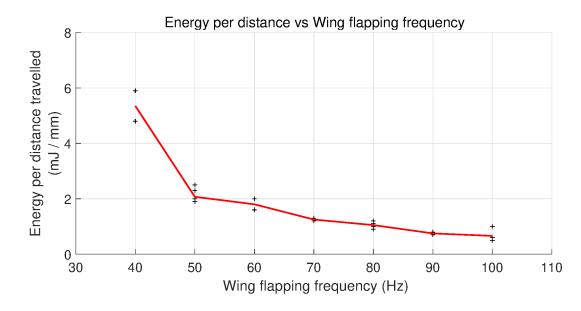


Fig. 22. The cost of transport (COT), the energy expended per unit distance traveled, decreases with increasing drive frequency f.

for hovering flight at a single position. The robot consumed approximately 50 mW measured power during hovering flight with feedback controlled attitude and position.

VI. FUTURE DIRECTIONS

Water locomotion can be further improved by performing a transition from water surface to airborne flight. We found that the vehicle was unable to lift off from the surface of the water simply by flapping its wings, as predicted by our earlier analysis indicating that the robot needs to lift approximately 9 times its own weight to break the water surface tension. In addition to explosive ejection [16], other potential means include: 1) electrowetting of the legs to reduce the contact

angle and therefore reduce the force [15], 2) creating waves on water surface with the help of flapping wings to lower the force required to break water surface film, 3) making the robot collide with an obstacle on the water surface which could provide the necessary impulse force.

As for ground locomotion, alternative modes such as jumping are possible. Hopping locomotion can be efficient due to advantageous scaling effects as robot size and weight are reduced [46], although additional weight and complicated hopping mechanisms are ill suited to honeybee-sized flying robots as discussed in Section III. Fei in [47] demonstrates bio-inspired jumping mechanisms and discusses the dynamics and optimization. Bhushan and Tomlin in [48] demonstrates an insect-sized microrobot capable of jumping 6 times per minute.

In order to lower the center of mass of the robot to facilitate passive stability in landing and avoid tipping over while performing ground and water surface locomotion, we re-oriented the actuators horizontally. We demonstrated the ability of the robot to hover about a point in space. While the lowered center of mass helped the robot to perform various modes of locomotion, the re-orientation increased the moments of inertia about pitch axis (Y-axis) and yaw axis (Z-axis), as compared to RoboBee [3]. The larger moment of inertia about the pitch axis reduced the authority over pitch control. To achieve higher pitch and yaw control authority and

maneuverability in any direction while hovering, the RoboFly is further modified in its newer version: Robofly-expanded [49], [50]. While maintaining the lowered center of mass, the actuators' long axes are now oriented sideways, along the pitch axis. This further re-orientation reduced the moment of inertia about the roll axis and improved the pitch control and the robot's maneuverability. A demonstration of controlled yaw motion in Robofly-expanded was reported in [50].

The locomotion of aquatic and semi-aquatic insects can be characterized using the thrust generating mechanism. The water surface locomotion shown by RoboFly is similar to most semiaquatic insects which utilize their hydrophobic legs for flotation and propulsion. This locomotion is known as water walking. Water walking insects also rely on surface tension for flotation as reviewed in [18]–[20]. Future insect-sized robots can explore other types of water surface locomotion observed in nature. The locomotion inspired by Marangoni propulsion of rove beetle and semiaquatic insects like Microvelia and Velia is reviewed in [20]. In this locomotion, the thrust is generated by uneven surface tension because of a chemical released by the insects. Honeybees, when trapped on the water surface, show a unique type of locomotion referred to as hydrofoiling locomotion by [51]. Honeybees are seen to be using their wings as hydrofoils to generate hydrodynamic thrust. Another interesting locomotion on water surface similar to honeybee's hydrofoiling locomotion is the rowing locomotion shown by the stonefly as reported in [52]. This locomotion makes use of both hydrodynamic drag as well as aerodynamic lift for propulsion.

The differential drag generated in the forward direction for the ground and the water surface locomotion can be estimated using a quasi-steady simulation of the flapping wings as was done in [50], [53]. Gravish and Wood in [53] validated these estimates using a 2-axis force sensor. The simulation can also be used to estimate the behavior of the forward drag and vertical lift as functions of the flapping frequency and amplitude. The legs can be further modified to achieve a more uniform coefficient of friction, which can be further used to predict the robot motion better. There are some known effects of flapping-wing flight [54], including viscosity, added mass, and the Kramer effect that can be incorporated in the three-dimensional simulations to accurately estimate the differential drag.

VII. CONCLUSION

This paper presents a new design with three major contributions to the field of insect-sized robotics. It 1) simplifies fabrication, 2) allows the robot to perform landing and ground locomotion, 3) designs legs for the robot to perform water surface locomotion similar to its biological counterparts.

In the new design, the airframe and transmission are all folded from a single multi-layer composite sheet. Compared to previous work, the design presented here represents an intermediate solution that lies between the many parts of [3], [29] and the single laminate sheet composed of many layers of [27] (Table I). We believe this represents a valuable intermediate between these two extremes because on the one

hand our design with two laminates gains many of the benefits of pop-up book manufacturing, such as having few parts and the ability to precision align small components. And on the other hand, it does not inherit the substantial complexity imposed by large number of interdependencies among layers. This reduces the difficulty of design iteration. Furthermore, we believe our intermediate approach is still amenable to automated manufacturing, by assuming that some steps will be performed by small robotic end-effectors. While simplifying the design by reducing the total number of distinct parts and improving the accuracy and precision during hand-assembly, we made sure that the pin joints made of Kapton film in transmission are identical to its earlier versions.

We showed that the lowered center of gravity of the robot allows it to land and ambulate along the ground including steering, in addition to flight. It was able to land consistently under feedback control and it was even able to land upright from an unstable open-loop flight. The cost of transport was found to be substantially higher than that of free-flight, so this mode of locomotion is better suited to precise motions, such as to precisely position a sensor. We additionally showed that ground ambulation can allow our robot to reach new places that are not accessible through flight, such as moving under a typical door. This represents a capability to negotiate an obstacle that heretofore exclusively the domain of the most adept ground robots, and impossible with air robots.

We also demonstrated another locomotive capability of the robot where it can, with the help of a set of three small horizontal legs, land on water surface and perform a waterlily beetle-like locomotion along the surface.

Our robot's multi-modal locomotion capabilities resemble those of larger robots. For example, [55] developed a larger bio-inspired robot (393 g, 72 cm) capable gliding flight as well as the ability to ambulate by rotating its ailerons. [56] developed a bio-inspired micro-vehicle (100 g, 30.5 cm) capable of performing aerial locomotion using wings and terrestrial locomotion using whegs. Similarly, [57] developed a bipedal ornithopter (11.4 g, 28 cm) with flapping wings for aerial locomotion and rotary legs for terrestrial locomotion. A 30 g robot took an approach similar to our robot by using the four propellers of its flight apparatus to steer its motion. These were used to steer a simple walking mechanism that was capable of moving in only one direction [58]. To our knowledge this work represents the first example of locomotion capability with three different modes at insect-scale.

A set of actuated legs for ground surface locomotion are used in other micro-robots such as the HAMR [59]. A miniaturized version of HAMR, the 22.5 mm long HAMR-Jr [60], demonstrated ground speed of nearly 14 body-lengths/second. HAMR recently demonstrated water locomotion both below and above the water surface and robustly managed the transition [15]. Even in miniaturized form, such quadrupedal robots require eight distinct actuators compared to RoboFly's two actuators, which manifests in the 320 mg weight compared to the 74 mg weight of RoboFly. While demonstrably more capable of handling uneven terrain, the weight of articulated leg mechanisms precludes flight in HAMR and HAMR-Jr. RoboFly's strategy for navigating uneven terrain or disturbances to the

water surface is fundamentally different: instead of dextrous ground or surface maneuvers, it is capable of brief hops or full flight above such obstacles. While flight is the primary locomotion mode of RoboFly, this work demonstrates three types of locomotion solely utilizing the vertical propulsion mechanism.

The capability of landing will allow the robot to perform intermittent flights. This will be useful for providing power to the robot. For example, the robot could more easily collect power from a laser because the laser would not have to follow it [24], [61], [62], or from magnetic resonance coupling, as has previously been demonstrated on a ground robot in [63]. Furthermore, landing will be necessary for the robot to collect energy from ambient energy sources such as indoor light or radio frequency signals such as WiFi [64] or cellular. In the case of energy harvesting from aeroelastic flutter [65], ground locomotion may be needed to position the robot in the flow. While these sources tend to be very minute and therefore insufficient to power larger robots, they may be enough to power the RoboFly for a reasonable fraction of the time, if it can land and charge between flights. The horizontal design of this work facilitates the attachment of power electronics [24] and sensors such as ultralight cameras [25].

ACKNOWLEDGMENT

This work is partially supported by the Air Force Office of Scientific Research under grant no. FA9550-14-1-0398. The authors also wish to thank Haripriya Vaidehi Narayanan, postdoctoral fellow, University of California Los Angeles for insightful discussions during the study on water surface locomotion.

REFERENCES

- [1] R. J. Wood, B. Finio, M. Karpelson, K. Ma, N. O. Pérez-Arancibia, P. S. Sreetharan, H. Tanaka, and J. P. Whitney, "Progress on 'pico'air vehicles," *The International Journal of Robotics Research*, vol. 31, no. 11, pp. 1292–1302, 2012.
- [2] W. S. Trimmer, "Microrobots and micromechanical systems," Sensors and actuators, vol. 19, no. 3, pp. 267–287, 1989.
- [3] K. Y. Ma, P. Chirarattananon, S. B. Fuller, and R. J. Wood, "Controlled flight of a biologically inspired, insect-scale robot," *Science*, vol. 340, no. 6132, pp. 603–607, 2013.
- [4] J. P. Whitney, P. S. Sreetharan, K. Y. Ma, and R. J. Wood, "Pop-up book mems," *Journal of Micromechanics and Microengineering*, vol. 21, no. 11, p. 115021, 2011.
- [5] P. Chirarattananon and R. J. Wood, "Identification of flight aerodynamics for flapping-wing microrobots," in *Robotics and Automation (ICRA)*, 2013 IEEE International Conference on. IEEE, 2013, pp. 1389–1396.
- [6] M. H. Dickinson and K. G. Gotz, "Unsteady aerodynamic performance of model wings at low reynolds numbers," *Journal of Experimental Biology*, vol. 174, no. 1, pp. 45–64, 1993.
- [7] M. H. Dickinson, F.-O. Lehmann, and S. P. Sane, "Wing rotation and the aerodynamic basis of insect flight," *Science*, vol. 284, no. 5422, pp. 1954–1960, 1999.
- [8] C. P. Ellington, "The aerodynamics of hovering insect flight. vi. lift and power requirements," *Phil. Trans. R. Soc. Lond. B*, vol. 305, no. 1122, pp. 145–181, 1984.
- [9] Z. A. Khan and S. K. Agrawal, "Design of flapping mechanisms based on transverse bending phenomena in insects," in *Robotics and Automation*, 2006. ICRA 2006. Proceedings 2006 IEEE International Conference on. IEEE, 2006, pp. 2323–2328.
- [10] P. Chirarattananon, K. Y. Ma, and R. J. Wood, "Adaptive control for takeoff, hovering, and landing of a robotic fly," in *Intelligent Robots and Systems (IROS)*, 2013 IEEE/RSJ International Conference on. IEEE, 2013, pp. 3808–3815.

- [11] M. Graule, P. Chirarattananon, S. Fuller, N. Jafferis, K. Ma, M. Spenko, R. Kornbluh, and R. Wood, "Perching and takeoff of a robotic insect on overhangs using switchable electrostatic adhesion," *Science*, vol. 352, no. 6288, pp. 978–982, 2016.
- [12] R. St. Pierre and S. Bergbreiter, "Toward autonomy in sub-gram terrestrial robots," *Annual Review of Control, Robotics, and Autonomous Systems*, vol. 2, pp. 231–252, 2019.
- [13] Y. S. Song and M. Sitti, "Surface-tension-driven biologically inspired water strider robots: Theory and experiments," *IEEE Transactions on robotics*, vol. 23, no. 3, pp. 578–589, 2007.
- [14] J.-S. Koh, E. Yang, G.-P. Jung, S.-P. Jung, J. H. Son, S.-I. Lee, P. G. Jablonski, R. J. Wood, H.-Y. Kim, and K.-J. Cho, "Jumping on water: Surface tension-dominated jumping of water striders and robotic insects," *Science*, vol. 349, no. 6247, pp. 517–521, 2015.
- [15] Y. Chen, N. Doshi, B. Goldberg, H. Wang, and R. J. Wood, "Controllable water surface to underwater transition through electrowetting in a hybrid terrestrial-aquatic microrobot," *Nature communications*, vol. 9, no. 1, p. 2495, 2018.
- [16] Y. Chen, H. Wang, E. F. Helbling, N. T. Jafferis, R. Zufferey, A. Ong, K. Ma, N. Gravish, P. Chirarattananon, M. Kovac et al., "A biologically inspired, flapping-wing, hybrid aerial-aquatic microrobot," *Science Robotics*, vol. 2, no. 11, p. eaao5619, 2017.
- [17] S. Zhou, W. Zhang, Y. Zou, X. Ke, F. Cui, and W. Liu, "Piezoelectric driven insect-inspired robot with flapping wings capable of skating on the water," *Electronics Letters*, vol. 53, no. 9, pp. 579–580, 2017.
- [18] D. L. Hu, B. Chan, and J. W. Bush, "The hydrodynamics of water strider locomotion," *Nature*, vol. 424, no. 6949, p. 663, 2003.
- [19] D. L. Hu and J. W. Bush, "The hydrodynamics of water-walking arthropods," *Journal of Fluid Mechanics*, vol. 644, pp. 5–33, 2010.
- [20] J. W. Bush and D. L. Hu, "Walking on water: biolocomotion at the interface," Annu. Rev. Fluid Mech., vol. 38, pp. 339–369, 2006.
- [21] H. Mukundarajan, T. C. Bardon, D. H. Kim, and M. Prakash, "Surface tension dominates insect flight on fluid interfaces," *Journal of Experi*mental Biology, vol. 219, no. 5, pp. 752–766, 2016.
- [22] B. Kwak and J. Bae, "Locomotion of arthropods in aquatic environment and their applications in robotics," *Bioinspiration & biomimetics*, vol. 13, no. 4, p. 041002, 2018.
- [23] Y. M. Chukewad, A. T. Singh, J. M. James, and S. B. Fuller, "A new robot fly design that is easier to fabricate and capable of flight and ground locomotion," in 2018 IEEE/RSJ International Conference on Intelligent Robots and Systems (IROS), Oct 2018, pp. 4875–4882.
- [24] J. James, V. Iyer, Y. Chukewad, S. Gollakota, and S. B. Fuller, "Liftoff of a 190 mg laser-powered aerial vehicle: The lightest wireless robot to fly," in 2018 IEEE International Conference on Robotics and Automation (ICRA). IEEE, 2018, pp. 1–8.
- [25] S. Balasubramanian, Y. M. Chukewad, J. M. James, G. L. Barrows, and S. B. Fuller, "An insect-sized robot that uses a custom-built onboard camera and a neural network to classify and respond to visual input," in 2018 7th IEEE International Conference on Biomedical Robotics and Biomechatronics (Biorob). IEEE, 2018, pp. 1297–1302.
- [26] S. B. Fuller, "Four wings: An insect-sized aerial robot with steering ability and payload capacity for autonomy," *IEEE Robotics and Automation Letters*, vol. 4, no. 2, pp. 570–577, 2019.
- Letters, vol. 4, no. 2, pp. 570–577, 2019.
 [27] P. S. Sreetharan, J. P. Whitney, M. D. Strauss, and R. J. Wood, "Monolithic fabrication of millimeter-scale machines," *Journal of Micromechanics and Microengineering*, vol. 22, no. 5, p. 055027, 2012.
- [28] R. J. Wood, "The first takeoff of a biologically inspired at-scale robotic insect," *IEEE transactions on robotics*, vol. 24, no. 2, pp. 341–347, 2008.
- [29] K. Y. Ma, S. M. Felton, and R. J. Wood, "Design, fabrication, and modeling of the split actuator microrobotic bee," in *Intelligent Robots* and Systems (IROS), 2012 IEEE/RSJ International Conference on. IEEE, 2012, pp. 1133–1140.
- [30] R. Steinmeyer, N. P. Hyun, E. F. Helbling, and R. J. Wood, "Yaw torque authority for a flapping-wing micro-aerial vehicle," in 2019 International Conference on Robotics and Automation (ICRA), May 2019, pp. 2481– 2487.
- [31] B. M. Finio, N. O. Pérez-Arancibia, and R. J. Wood, "System identification and linear time-invariant modeling of an insect-sized flapping-wing micro air vehicle," in 2011 IEEE/RSJ International Conference on Intelligent Robots and Systems. IEEE, 2011, pp. 1107–1114.
- [32] M. Rubenstein, C. Ahler, and R. Nagpal, "Kilobot: A low cost scalable robot system for collective behaviors," in 2012 IEEE International Conference on Robotics and Automation. IEEE, 2012, pp. 3293–3298.
- [33] H. H. Hariri, G. S. Soh, S. Foong, and K. Wood, "Locomotion study of a standing wave driven piezoelectric miniature robot for bi-directional motion," *Ieee Transactions on robotics*, vol. 33, no. 3, pp. 742–747, 2017.

- [34] Y. Wu, J. K. Yim, J. Liang, Z. Shao, M. Qi, J. Zhong, Z. Luo, X. Yan, M. Zhang, X. Wang et al., "Insect-scale fast moving and ultrarobust soft robot," Science Robotics, vol. 4, no. 32, p. eaax1594, 2019.
- [35] "Autonomous Insect Robotics Laboratory, University of Washington," Available: http://depts.washington.edu/airlab/IROS2018-1906. html. 2018.
- [36] A. Singh, T. Libby, and S. B. Fuller, "Rapid inertial reorientation of an aerial insect-sized robot using a piezo-actuated tail," in 2019 International Conference on Robotics and Automation (ICRA). IEEE, 2019, pp. 4154–4160.
- [37] S. B. Fuller, M. Karpelson, A. Censi, K. Y. Ma, and R. J. Wood, "Controlling free flight of a robotic fly using an onboard vision sensor inspired by insect ocelli," *Journal of The Royal Society Interface*, vol. 11, no. 97, p. 20140281, 2014.
- [38] "Autonomous Insect Robotics Laboratory, University of Washington," Available: http://depts.washington.edu/airlab/RoboFly_hovering.html, 2019.
- [39] P. Chirarattananon, K. Y. Ma, and R. J. Wood, "Adaptive control for takeoff, hovering, and landing of a robotic fly," in 2013 IEEE/RSJ International Conference on Intelligent Robots and Systems. IEEE, 2013, pp. 3808–3815.
- [40] J. B. Keller, "Surface tension force on a partly submerged body," *Physics of Fluids*, vol. 10, no. 11, pp. 3009–3010, 1998.
- [41] E. Mansfield, H. Sepangi, and E. Eastwood, "Equilibrium and mutual attraction or repulsion of objects supported by surface tension," Philosophical Transactions of the Royal Society of London. Series A: Mathematical, Physical and Engineering Sciences, vol. 355, no. 1726, pp. 869–919, 1997.
- [42] "Robofly landing on the water surface," Available: https://youtu.be/ EZ6O-4xPch8, 2020.
- [43] J. James and S. B. Fuller, "A high-voltage power electronics unit for flying insect robots that can modulate wing thrust," in 2021 IEEE International Conference on Robotics and Automation (ICRA). IEEE, 2021 [accepted].
- [44] N. T. Jafferis, E. F. Helbling, M. Karpelson, and R. J. Wood, "Untethered flight of an insect-sized flapping-wing microscale aerial vehicle," *Nature*, vol. 570, no. 7762, p. 491, 2019.
- [45] M. Karpelson, G.-Y. Wei, and R. J. Wood, "Driving high voltage piezoelectric actuators in microrobotic applications," *Sensors and actuators A: Physical*, vol. 176, pp. 78–89, 2012.
- [46] R. M. Alexander, Principles of animal locomotion. Princeton University Press, 2003.
- [47] F. Li, W. Liu, X. Fu, G. Bonsignori, U. Scarfogliero, C. Stefanini, and P. Dario, "Jumping like an insect: Design and dynamic optimization of a jumping mini robot based on bio-mimetic inspiration," *Mechatronics*, vol. 22, no. 2, pp. 167–176, 2012.
- [48] P. Bhushan and C. Tomlin, "An insect-scale untethered laser-powered jumping microrobot," *arXiv preprint arXiv:1908.03282*, 2019.
- [49] D. Dhingra, Y. M. Chukewad, and S. B. Fuller, "A device for rapid, automated trimming of insect-sized flying robots," *IEEE Robotics and Automation Letters*, vol. 5, no. 2, pp. 1373–1380, 2020.
- [50] Y. M. Chukewad and S. Fuller, "Yaw control of a hovering flappingwing aerial vehicle with a passive wing hinge," *IEEE Robotics and Automation Letters*, 2021.
- [51] C. Roh and M. Gharib, "Honeybees use their wings for water surface locomotion," *Proceedings of the National Academy of Sciences*, 2019.
- [52] J. H. Marden and M. A. Thomas, "Rowing locomotion by a stonefly that possesses the ancestral pterygote condition of co-occurring wings and abdominal gills," *Biological Journal of the Linnean Society*, vol. 79, no. 2, pp. 341–349, 2003.
- [53] N. Gravish and R. J. Wood, "Anomalous yaw torque generation from passively pitching wings," in 2016 IEEE International Conference on Robotics and Automation (ICRA). IEEE, 2016, pp. 3282–3287.
- [54] S. P. Sane, "The aerodynamics of insect flight," *Journal of experimental biology*, vol. 206, no. 23, pp. 4191–4208, 2003.
- [55] L. Daler, S. Mintchev, C. Stefanini, and D. Floreano, "A bioinspired multi-modal flying and walking robot," *Bioinspiration & biomimetics*, vol. 10, no. 1, p. 016005, 2015.
- [56] R. J. Bachmann, F. J. Boria, R. Vaidyanathan, P. G. Ifju, and R. D. Quinn, "A biologically inspired micro-vehicle capable of aerial and terrestrial locomotion," *Mechanism and Machine Theory*, vol. 44, no. 3, pp. 513– 526, 2009.
- [57] K. Peterson and R. S. Fearing, "Experimental dynamics of wing assisted running for a bipedal ornithopter," in *Intelligent Robots and Systems* (IROS), 2011 IEEE/RSJ International Conference on. IEEE, 2011, pp. 5080–5086.

- [58] Y. Mulgaonkar, B. Araki, J.-s. Koh, L. Guerrero-Bonilla, D. M. Aukes, A. Makineni, M. T. Tolley, D. Rus, R. J. Wood, and V. Kumar, "The flying monkey: a mesoscale robot that can run, fly, and grasp," in *Robotics and Automation (ICRA)*, 2016 IEEE International Conference on. IEEE, 2016, pp. 4672–4679.
- [59] B. Goldberg, N. Doshi, K. Jayaram, and R. J. Wood, "Gait studies for a quadrupedal microrobot reveal contrasting running templates in two frequency regimes," *Bioinspiration & biomimetics*, vol. 12, no. 4, p. 046005, 2017.
- [60] K. Jayaram, J. Shum, S. Castellanos, E. F. Helbling, and R. J. Wood, "Scaling down an insect-size microrobot, hamr-vi into hamr-jr," in 2020 IEEE International Conference on Robotics and Automation (ICRA), 2020, pp. 10305–10311.
- [61] V. Iyer, E. Bayati, R. Nandakumar, A. Majumdar, and S. Gollakota, "Charging a smartphone across a room using lasers," *Proceedings of the ACM on Interactive, Mobile, Wearable and Ubiquitous Technologies*, vol. 1, no. 4, p. 143, 2018.
- [62] T. J. Nugent and J. T. Kare, "Laser power beaming for defense and security applications," in *Unmanned systems technology XIII*, vol. 8045. International Society for Optics and Photonics, 2011, p. 804514.
- [63] M. Karpelson, B. H. Waters, B. Goldberg, B. Mahoney, O. Ozcan, A. Baisch, P.-M. Meyitang, J. R. Smith, and R. J. Wood, "A wirelessly powered, biologically inspired ambulatory microrobot," in *Robotics and Automation (ICRA)*, 2014 IEEE International Conference on. IEEE, 2014, pp. 2384–2391.
- [64] V. Talla, B. Kellogg, B. Ransford, S. Naderiparizi, S. Gollakota, and J. R. Smith, "Powering the next billion devices with wi-fi," in *Proceedings of the 11th ACM Conference on Emerging Networking Experiments and Technologies*. ACM, 2015, p. 4.
- [65] M. Bryant, E. Wolff, and E. Garcia, "Aeroelastic flutter energy harvester design: the sensitivity of the driving instability to system parameters," *Smart Materials and Structures*, vol. 20, no. 12, p. 125017, 2011.



Yogesh Chukewad received the Ph.D. in Mechanical Engineering from the University of Washington, Seattle, WA, USA in 2020. He is currently working as a Mechatronics Engineer in California.

His research interests include design and controls of micro-robots, sensor fusion, and localization for autonomous robots.



Johannes James received the B.S. in mechanical engineering from the California Maritime Academy C.S.U. in Vallejo, California, U.S.A. in 2013. He is currently working toward power autonomous flapping wing insect robots pursuant to the Ph.D. degree in the Mechanical Engineering dept. at the University of Washington.

His research interests include industrial automation and control, embedded systems, micro-robotics, and power electronics.



Avinash Singh received his B.E. in mechanical engineering from Nagpur University, India in 2013 and his M.S. in mechanical engineering from the University of Washington, Seattle, WA, USA in 2018. He is currently working as a robotics engineer in Seattle, WA.

His research interests include autonomous robotics, bio-inspired robotics, aerial robotics, SLAM and machine learning.



Sawyer Fuller, Assistant Professor of Mechanical Engineering, creates biologically-inspired sensors, control systems, and mechanical designs targeted at insect-sized air and ground vehicles, and investigates the flight systems of aerial insects. He completed his Ph.D. in Biological Engineering at the California Institute of Technology and B.S. and M.S. degrees in Mechanical Engineering at the Massachusetts Institute of Technology, and postdoctoral training at Harvard. In addition to his work in insect flight control, he also developed a frog-hopping robot at

the NASA Jet Propulsion Laboratory and invented an ink-jet printer capable of fabricating millimeter-scale 3D metal machines at the MIT Media Lab.